IEEE Robotics and Automation Letters (RA-L) paper, presented at ICRA 2026, Vienna, Austria. Cite as RA-L paper.

Semi-Autonomous Teleoperation Using Differential Flatness of a Crane Robot for Aircraft In-Wing Inspection

Wade Marquette, Kyle Schultz, Vamsi Jonnalagadda, Benjamin Wong, *Graduate Student Member, IEEE*, Joseph Garbini, and Santosh Devasia, *Fellow, IEEE*

***Abstract*—Visual inspection of confined spaces such as aircraft wings is ergonomically challenging for human mechanics. This work presents a novel crane robot that can travel the entire span of the aircraft wing, enabling mechanics to perform inspection from outside of the confined space. However, teleoperation of the crane robot can still be a challenge due to the need to avoid obstacles in the workspace and potential oscillations of the camera payload. The main contribution of this work is to exploit the differential flatness of the crane-robot dynamics for designing reduced-oscillation, collision-free time trajectories of the camera payload for use in teleoperation. Autonomous experiments verify the efficacy of removing undesired oscillations by 89%. Furthermore, teleoperation experiments demonstrate that the controller eliminated collisions (from 33% to 0%) when 12 participants performed an inspection task with the use of proposed trajectory selection when compared to the case without it. Moreover, even discounting the failures due to collisions, the proposed approach improved task efficiency by 18.7% when compared to the case without it.**

***Index Terms*—Telerobotics and teleoperation, collision avoidance, inspection robots, manufacturing.**

I. Introduction

CONFINED-space inspection is a major aspect of aerospace manufacturing and maintenance, especially inside aircraft wings (where fuel is stored), which are ergonomically challenging, hazardous environments to work in. For example, mechanics need to don protective suits and respirators for safety in such spaces, which makes the work cumbersome [1]. Moreover, ensuring safety requires regular check-ins from an outside partner. These difficulties of operating in confined spaces motivate the development of robotic solutions that allow mechanics to perform their work from outside the confined space. A challenge with typical robotic inspection solutions is that they require repeated time-consuming installation and removal for each of the many separated internal structure segments (bays, see Fig. 1) of the wing in commercial aircraft architectures. An additional challenge is that teleoperation (which takes advantage of human expertise to perform complex tasks) can be slow since it is difficult for humans to manage multiple tasks such as (i) inspection of the space and (ii) avoiding obstacles – especially, in complex confined spaces. This work presents a robotic inspection system that can move through the entire wing without re-installation in each bay and develops a control system to aid collision avoidance and thereby, improve teleoperation performance.

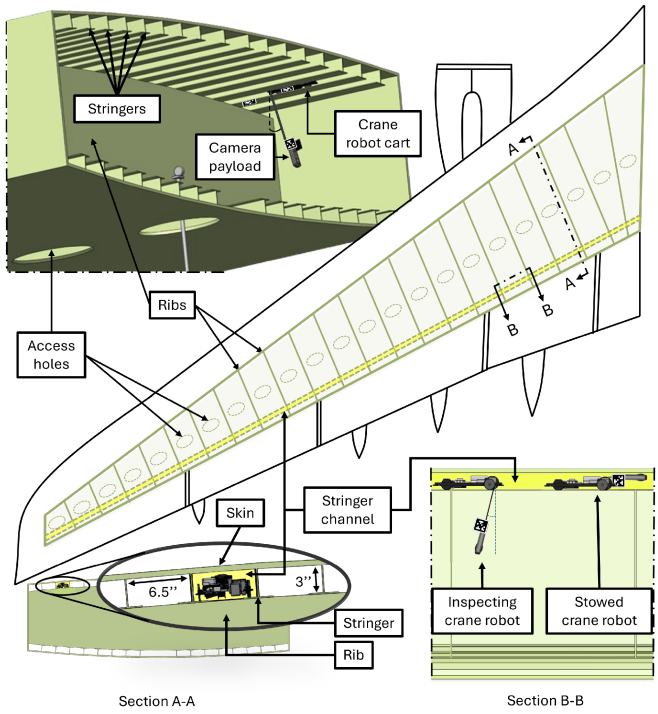

Fig. 1. The crane robot can inspect the entire wing by traversing stringer channels. (Top-left) Partial view of an aircraft wing bay with crane robot moving inside the channel between two stringers, suspending a camera payload for inspection. The wing bays are partitioned into separate spaces by ribs and each space is typically accessed through narrow access holes. (Center) A two-dimensional schematic of the wing with a sample stringer channel highlighted in yellow, spanning the length of the wing, which provides access (over the ribs, with the camera stowed) between adjacent bays. (Bottom left, Section A-A) Cross section with the stowed crane robot in the stringer channel (highlighted in yellow) formed below the upper skin and between adjacent stringers enabling passage over the ribs. (Bottom right, Section B-B) Crane robot in the stringer channel (yellow highlight).

Received 16 September 2024; accepted 14 January 2025. Date of publication 29 January 2025; date of current version 10 February 2025. This article was recommended for publication by Associate Editor Thomas Hulin and Editor Jee-Hwan Ryu upon evaluation of the reviewers' comments. This work was supported by the University of Washington Institutional Review Board under Grant STUDY00021303. *(Corresponding author: Santosh Devasia.)*

The authors are with the Mechanical Engineering Department, University of Washington, Seattle, WA 98195 USA (e-mail: wm25@uw.edu; kylews@uw.edu; jnvk@uw.edu; bycw@uw.edu; garbini@uw.edu; devasia@uw.edu).

This letter has supplementary downloadable material available at https://doi.org/10.1109/LRA.2025.3536207, provided by the authors.

Digital Object Identifier 10.1109/LRA.2025.3536207

IEEE Robotics and Automation Letters (RA-L) paper, presented at ICRA 2026, Vienna, Austria. Cite as RA-L paper.

The current work avoids the problem of installation/removal in each of the separate bays by designing a compact robot that can fit and move inside the channel between stringers, and thereby, access the entirety of the wing operating akin to a gantry crane with a suspended camera as the payload. The camera can be retracted to cross the ribs that separate adjacent bays. Additionally, to aid teleoperation, this work reduces motion-induced oscillations and automates collision avoidance during teleoperation of the crane robot. In particular, the differential flatness of the crane-robot dynamics is used to design reduced-oscillation, collision-free time trajectories of the camera payload. The resulting teleoperation controller allows the operator to directly specify camera payload trajectories while autonomously avoiding large oscillations and potential collisions. Experimental evaluations show that the teleoperation assistance reduces undesired oscillation by 89% and user trials of 12 participants demonstrate the mitigation of collision and an 18.7% improvement in task completion time when neglecting collision compared to the case without the teleoperation assistance.

II. Related Works

A. Design of Robots for Confined Spaces

Currently available confined space robotic solutions cannot access the entire wing during manufacturing of the commercial aircraft architecture. For example, conventional manipulator-based, continuum-type, and snake robot architectures for confined space inspection [2], hole cleaning [3], and multi-tasks [4] within aircraft wings cannot move between bays through the ribs over the span of the wing and require manual installation and removal for each bay. Movement between bays is achieved with the Eeloscope [1] by swimming through holes in the ribs when fuel is present inside aircraft wing tanks. However, this solution is not applicable in the absence of fuel, e.g., during initial aircraft manufacturing. Another approach is using mobile robots that drive through rib cutouts in aircraft wings if the driving surfaces are smooth [5], but this solution does not apply to larger aircraft with uneven surfaces due to stiffening stringer structures on the inner-skin. The crane robot overcomes the challenge of traversing separated bays by using a small cross-sectional area to traverse the bays through narrow (6.5 in $\times$ 3 in) stringer channels that span the entire wing. Previous works have introduced robots to move in narrow spaces such as pipes and channels, e.g., snake [6] and inchworm [7] robots. However, these designs rely on the entire cross section to be continuous, but the stringer channels tend to be open away from the skin. Therefore, this work presents a novel crane robot that uses wheels to stay inside the stringer channel, similar to wheeled pipe crawling robots [8]. Moreover, the crane robot exploits the opening in the stringer channel to suspend a camera via a pulley mechanism to perform inspection tasks, as shown in Fig. 1. In inspection tasks, trajectory tracking is critical to move the payload camera along a desired path, which is different from the goal in traditional gantry cranes used in the aerospace industry that seek to move objects from one point to another.

B. Assisting Teleoperation in Complex Environments

The crane robot (with controls to position on the stringer channel and the camera position) is analogous to a variable-length gantry crane [9]. Therefore, it shares similar challenges in teleoperation as industrial crane systems, where the operator controls both the cart position and the cable length independently [9]. This conventional control approach, where the operator specifies trajectories that do not cause undesired oscillations of the payload, can be challenging and require extensive training to learn how to manage the gantry-crane dynamics. To avoid such challenges in teleoperation, this work develops a semi-autonomous teleoperation control for the crane robot, which can make teleoperation easier as shown in [10]. The human operator only specifies a reference point to generate trajectories for the camera payload, and handling of control complexities such as obstacle avoidance and unwanted oscillations (due to payload dynamics) is managed autonomously to assist teleoperation. Input shaping is a widely used method to reduce residual oscillations in crane positioning [11]. However, input shaping does not ensure payload trajectory tracking, which is important near obstacles in confined spaces. Alternatively, gantry cranes have been shown to be differentially flat, allowing all states and inputs to be represented as functions of the output and its time derivatives [12]. This work leverages the differential flatness property of the crane-robot dynamics as the basis of the teleoperation assistance where camera payload coordinates are considered as the output [13], [14]. Previous work has shown that flatness-based control can reject undesired payload oscillations caused by disturbances during autonomous trajectory tracking and positioning [15]. In addition to crane applications, differential flatness has been widely applied to a variety of systems, including cable-suspended UAV path planning [16], UAV-UGV cooperative landing [17], and aerobatic trajectories of VTOL aircraft [18]. These autonomous applications are based on predefined trajectories or objectives but do not address real-time trajectory generation to assist avoiding obstacles during human teleoperation. Specifically, the proposed crane-robot assistance modulates the operator's reference input to avoid collisions, and additionally, since the low-order polynomial trajectory is tracked accurately, the approach also reduces unwanted oscillations. Previous works have used the flatness-based approach for gantry crane teleoperation using sufficiently-smooth online S-curve velocity trajectory generation. However, this approach is used in an environment without obstacles [19]. Moreover, this approach relies on a fixed-length payload and a linearized model, which may not be sufficiently accurate for crane robot operations, where varying payload lengths and rapid movements can cause larger swing angles. Therefore, this proposed work develops a trajectory generation approach for the gantry-crane model using the differential flatness of the dynamics, which accounts for both (i) the nonlinearity due to the swing dynamics and (ii) the variable length. Thus, the proposed approach enables easier (collision-free and reduced-oscillation), semi-autonomous teleoperation of the crane robot, which in turn, improves operator performance during confined-space inspection.

III. Crane Robot Description

To deploy inside the narrow stringer channel formed by the flanges of the stringer and the wing skin, in Fig. 1, the crane robot frame is segmented into two smaller pieces which are subsequently attached (once inside the stringer channel) with a threaded rod. This allows installation through the narrow gap of the stringer channel while being wide enough to drive on the flanges as as depicted in Fig. 2(a). Once installed, the crane robot drives through the channel on four vertical wheels with one wheel driven by a motor. The crane robot has four side wheels,

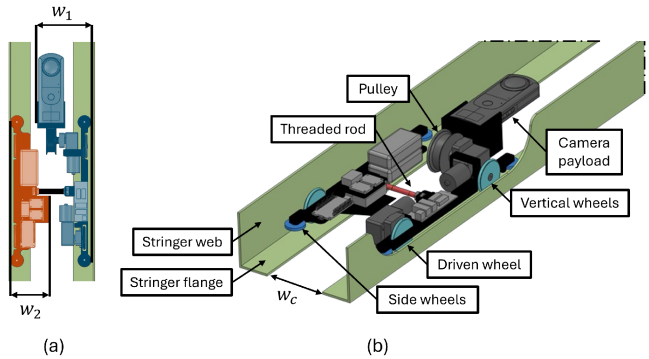

Fig. 2. Installation of the crane robot in the stinger channel. (a) The crane robot frame segmented in two pieces with widths $w_1 = 3.75$ in and $w_2 = 2.75$ in and thickness less than 2.5in so each segment can be installed diagonally through the channel opening of width $w_c = 3.5$ in. (b) The installation is completed by connecting the segmented frame with a threaded rod (red). The width of the connected segments is larger than the channel opening width, w_c, enabling the crane robot to drive on the stringer flanges with its vertical wheels (cyan) while its side wheels (blue) contact the stringer web to correct channel misalignment.

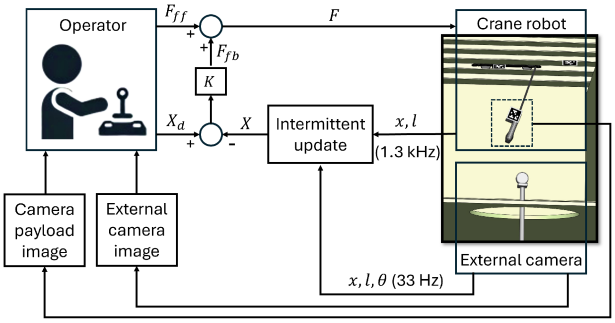

Fig. 3. Crane-robot's control scheme. The external camera at the access hole measures the cart position, x, the payload length, l, and the swing angle, θ, from the fiducial markers at a sampling rate of 33 Hz, which intermittently updates feedback collected from the motor encoders at a sampling rate of 1.3 kHz to construct the crane robot's states, X. From the operator workstation, the feedforward input, F_{ff}, and desired states, X_d, are specified through a joystick interface by the operator observing the external camera and camera payload image. The combined feedforward force, F_{ff}, and feedback force, F_{fb}, is the applied crane-robot input, F.

shown in Fig. 2(b), which can contact the stringer webs and help realign the crane robot with the stringer channel.

The crane robot performs inspection tasks by suspending a camera into the confined space using a pulley mechanism. To traverse adjacent bays, the camera payload is stowed and released from the channel by wrapping and unwrapping the camera around the pulley. The crane robot deploys a wireless 360 camera payload, enabling the operator to perform remote inspection in any direction by panning a tablet application, similar to such use in other applications such as power-line inspection robots [20].

Operators receive overall perspective of the environment using an external camera to reduce disorienting effects associated with system movement of the robot's onboard camera [21]. Specifically, an external camera, located at the access hole, provides an external view of both the crane robot and obstacles, delivering situational awareness to the operator shown in Fig. 3. The external camera also provides vision-based state and output feedback using fiducial markers (Apriltags [22]) located on the crane-robot's cart and camera payload along with a reference tag located in the confined space for tracking control, e.g., as in [23].

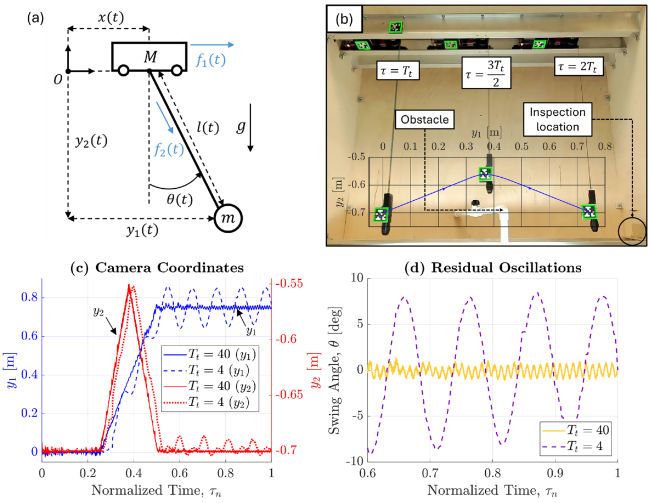

Fig. 4. Comparison of residual oscillations for slow and fast trajectories, without swing-dynamics compensation. (a) The crane-robot schematic: inputs are the force on the cart, f_1, and the force on the payload, f_2; outputs are the horizontal and vertical payload-positions, y_1 and y_2, respectively; and states are are the cart's position, x, the payload length, l, and the payload swing angle, θ, along with their time derivatives. (b) Snapshots of the crane robot prototype traversing a ramp-like trajectory which transitions the camera payload over a pipeline obstacle near an inspection location. (c) Comparative time responses of the outputs y_1, y_2, for two different transition times, $T_t = 4$ and $T_t = 40$ seconds, plotted against normalized time, $\tau_n = \frac{\tau}{4T_t}$. (d) Residual oscillations at the inspection point for the two transition times.

Measurements from the fiducial markers provide swing angle information and global-correction updates for crane-position and payload-length estimates from motor encoders. Operators use camera feedback to visualize the pose of the crane robot and use a joystick, as in industrial crane control [24], to send wireless, horizontal-and-vertical, camera-payload velocity commands.

IV. Control Problem Formulation

The dynamics of the crane robot resembles those of a variable-length gantry crane, as depicted in Fig. 4(a). Under low-speed operations, it is feasible to neglect the payload swing, θ, dynamics. Without the swing dynamics, the horizontal position, y_1, of the payload (inspection camera) corresponds to the cart position, x, and the vertical camera position, y_2, corresponds to the payload length, l. As a result, the outputs (the horizontal y_1 and vertical y_2 positioning of the camera) are decoupled from each other and can be controlled independent of each other.

The decoupled approach, without compensating for the swing dynamics (i.e. assuming $x = y_1$ and $l = -y_2$), can lead to acceptable tracking during low-speed operation. To illustrate, tracking is studied for a ramp-like trajectory to move across the confined space over a pipeline obstacle, as shown in Fig. 4(b). The nominal desired trajectory, $\tilde{Y} = \begin{bmatrix}\tilde{y}_1(\tau) & \tilde{y}_2(\tau)\end{bmatrix}^T$, is defined by

$$\tilde{Y} = \begin{cases} \begin{bmatrix}0 & 0\end{bmatrix}^T & 0 \le \tau < T_t \\ \begin{bmatrix}\frac{\Delta y_1}{T_t}(\tau - T_t) & \frac{2\Delta y_2}{T_t}(\tau - T_t)\end{bmatrix}^T & T_t \le \tau < \frac{3}{2}T_t \\ \begin{bmatrix}\frac{\Delta y_1}{T_t}(\tau - T_t) & -\frac{2\Delta y_2}{T_t}(\tau - 2T_t)\end{bmatrix}^T & \frac{3}{2}T_t \le \tau < 2T_t \\ \begin{bmatrix}\Delta y_1 & 0\end{bmatrix}^T & 2T_t \le \tau < 4T_t \end{cases},$$

IEEE Robotics and Automation Letters (RA-L) paper, presented at ICRA 2026, Vienna, Austria. Cite as RA-L paper.

where the transition time, T_t, defines the duration of movement, Δy_1 defines the change in the camera's horizontal position over T_t, and Δy_2 defines the change in the camera's vertical position over $\frac{T_t}{2}$ before returning to the initial position within $\frac{T_t}{2}$. The nominal time trajectories $\tilde{y}_1$ and $\tilde{y}_2$ are smoothed by four cascaded first-order low-pass filters with a cutoff frequency, α, as $y_1(\tau) = F_f \tilde{y}_1$ and $y_2(\tau) = F_f \tilde{y}_2$, with $F_f = (\frac{\alpha}{\lambda+\alpha})^4$ where λ represents the Laplace variable.

The response of the crane robot with cart mass, $M = 0.815$ kg, and payload mass, $m = 0.225$ kg, when following the time trajectories $y_1(\tau)$ and $y_2(\tau)$, parameterized by $\Delta y_1 = 0.75$ m, $\Delta y_2 = 0.15$ m, and $\alpha = 10$ $\frac{\text{rad}}{\text{s}}$ (1.59 Hz) at a slow transition time of T_t of 40 seconds, by tracking the decoupled commands of the cart and payload length are shown in Fig. 4(c). Residual oscillations, present after reaching the inspection point, are small and remain below a magnitude of 1.4 degrees, as shown in Fig. 4(d). However, this decoupling of the payload positioning is only valid at low speeds and accelerations, and rapid changes in the positions (e.g., needed for faster movements to speed up inspection) can excite the swing dynamics, inducing significant oscillations, which in turn, can make teleoperation challenging. The swing dynamics are excited as the same ramp-like trajectory is tracked with a smaller transition time, $T_t = 4$ seconds, with a 6.5 times increase in residual oscillation magnitude to 9.1 degrees, as shown in Fig. 4(c) and (d). Such large residual oscillations need to be avoided to enable fast teleoperation. Therefore, the research problem is to compensate for the swing dynamics to reduce residual oscillations.

V. Flatness-Based Semi-Autonomous Control

A. Flatness-Based Feedforward Inputs

The dynamics of the crane robot can be modeled in state space X as [15], [25]

$$\frac{d}{dt}X = \begin{bmatrix} \dot{x} \\ 0 \\ \dot{\theta} \\ -\frac{2}{l}\dot{l}\dot{\theta} - \frac{g}{l}s \\ \dot{l} \\ l\dot{\theta}^2 + gc \end{bmatrix} + \begin{bmatrix} 0 & 0 \\ \frac{1}{M} & \frac{-s}{M} \\ 0 & 0 \\ \frac{-c}{Ml} & \frac{sc}{Ml} \\ 0 & 0 \\ \frac{-s}{M} & \left(\frac{s^2}{M} + \frac{1}{m}\right) \end{bmatrix} \begin{bmatrix} f_1 \\ f_2 \end{bmatrix}, \quad (1)$$

where where M is the mass of the cart, m is the mass of the payload, f_1 is the cart force, f_2 is the payload force, g is the gravitational acceleration, $s = \sin(\theta(t))$, $c = \cos(\theta(t))$, state vector $X = \begin{bmatrix} x & \dot{x} & \theta & \dot{\theta} & l & \dot{l} \end{bmatrix}^T$ and it is assumed that the rolling friction on the cart is negligible, or has been compensated. The outputs of the system are the camera's horizontal position, y_1, and vertical position, y_2, which can be expressed in terms of the crane-robot states (x, l, θ) as

$$Y = \begin{bmatrix} y_1 \\ y_2 \end{bmatrix} = \begin{bmatrix} x + ls \\ -lc \end{bmatrix}. \quad (2)$$

To enable tracking of the outputs (y_1, y_2), an expression relating the input forces (f_1 and f_2) to the outputs is found by differentiating the outputs until the inputs appears [14]. Specifically, differentiating (2) twice results in

$$\dot{Y} = \begin{bmatrix} \dot{y}_1 \\ \dot{y}_2 \end{bmatrix} = \begin{bmatrix} \dot{x} + \dot{l}s + l\dot{\theta}c \\ -\dot{l}c + l\dot{\theta}s \end{bmatrix} \quad (3)$$

$$\ddot{Y} = \begin{bmatrix} \ddot{y}_1 \\ \ddot{y}_2 \end{bmatrix} = \begin{bmatrix} \ddot{x} + \ddot{l}s + 2\dot{l}\dot{\theta}c + l\ddot{\theta}c - l\dot{\theta}^2 s \\ -\ddot{l}c + 2\dot{l}\dot{\theta}s + l\ddot{\theta}s + l\dot{\theta}^2 c \end{bmatrix}. \quad (4)$$

The second time derivative $\ddot{Y}$ depends on the inputs (f_1, f_2) since substituting for the second derivatives of the states from (1) into (4) results in

$$\begin{bmatrix} \ddot{y}_1 \\ \ddot{y}_2 \end{bmatrix} = \begin{bmatrix} 0 \\ -g \end{bmatrix} + \begin{bmatrix} 0 & \frac{s}{m} \\ 0 & -\frac{c}{m} \end{bmatrix} \begin{bmatrix} f_1 \\ f_2 \end{bmatrix} = \begin{bmatrix} 0 \\ -g \end{bmatrix} + \tilde{\beta} F, \quad (5)$$

where $\tilde{\beta}$ is defined as the matrix of terms preceding the input vector $F = \begin{bmatrix} f_1 & f_2 \end{bmatrix}^T$. However, the force F cannot be found from (5) since the matrix $\tilde{\beta}$ is not invertible. Therefore, assuming that the input f_2 is sufficiently smooth, and redefining the new input to be $\dot{f}_2$ (with f_2 considered as an extended state), the output expression in (5) is differentiated again to obtain

$$Y^{(3)} = \begin{bmatrix} y_1^{(3)} \\ y_2^{(3)} \end{bmatrix} = \frac{1}{m} \begin{bmatrix} f_2 \dot{\theta} c \\ f_2 \dot{\theta} s \end{bmatrix} + \tilde{\beta} \begin{bmatrix} f_1 \\ \dot{f}_2 \end{bmatrix}, \quad (6)$$

where the superscript in brackets (i) indicates the ith time derivative, e.g., $y_k^{(i)}$ denotes ith time derivative of y_k for $k \in \{1, 2\}$. Again, the redefined input $(f_1, \dot{f}_2)$ cannot be found from (6) since the matrix $\tilde{\beta}$ is not invertible. Therefore, the input is further redefined to be $\ddot{f}_2$, with extended states $(f_2, \dot{f}_2)$, and differentiating (6) again to obtain

$$Y^{(4)} = \begin{bmatrix} y_1^{(4)} \\ y_2^{(4)} \end{bmatrix} = \frac{1}{m} \begin{bmatrix} \ddot{f}_2 s + 2\dot{f}_2 \dot{\theta} c + f_2 \ddot{\theta} c - f_2 \dot{\theta}^2 s \\ -\ddot{f}_2 c + 2\dot{f}_2 \dot{\theta} s + f_2 \ddot{\theta} s + f_2 \dot{\theta}^2 c \end{bmatrix}. \quad (7)$$

Substituting for the second derivatives of the states from (1) into (7), and arranging yields

$$\begin{bmatrix} y_1^{(4)} \\ y_2^{(4)} \end{bmatrix} = \frac{1}{m} \begin{bmatrix} -\frac{1}{Ml} f_2 c^2 & s \\ -\frac{1}{Ml} f_2 cs & -c \end{bmatrix} \begin{bmatrix} f_1 \\ \ddot{f}_2 \end{bmatrix} - \frac{1}{m} \begin{bmatrix} -2\dot{f}_2 \dot{\theta} c + f_2 \dot{\theta}^2 s - \frac{1}{Ml} f_2^2 sc^2 + \frac{2}{l} f_2 \dot{l} \dot{\theta} c + \frac{g}{l} f_2 sc \\ -2\dot{f}_2 \dot{\theta} s - f_2 \dot{\theta}^2 c - \frac{1}{Ml} f_2^2 s^2 c + \frac{2}{l} f_2 \dot{l} \dot{\theta} s + \frac{g}{l} f_2 s^2 \end{bmatrix}. \quad (8)$$

The final redefined input $(f_1, \ddot{f}_2)$ can be found from (8) if the matrix β

$$\beta = \begin{bmatrix} -\frac{1}{Ml} f_2 c^2 & s \\ -\frac{1}{Ml} f_2 cs & -c \end{bmatrix} \quad (9)$$

preceding the input vector $\begin{bmatrix} f_1 & \ddot{f}_2 \end{bmatrix}^T$ is invertible. The determinant of β is $\frac{f_2 c}{Ml}$, making it invertible provided the un-stowed payload length is nonzero, $l \neq 0$, the payload swing angle does not become horizontal, $\theta \in (-\frac{\pi}{2}, \frac{\pi}{2})$, and the payload force remains negative, $f_2 < 0$ to ensure that the cable remains taut. Given the desired outputs' fourth derivatives, $Y_d^{(4)}$, the redefined input f_1 and $\ddot{f}_2$, can be found by settling the right hand side of (8) to be $\begin{bmatrix} v_1 & v_2 \end{bmatrix}^T$ leading to the system $y_1^{(4)} = v_1$, $y_2^{(4)} = v_2$.

Here, the feedforward inputs $f_{1,ff}$ and $\ddot{f}_{2,ff}$ can be found by setting $v_1 = y_{1,d}^{(4)}$ and $v_2 = y_{2,d}^{(4)}$

$$f_{1,ff} = \frac{Ml}{f_2 c} \left(-m(cy_{1,d}^{(4)} + sy_{2,d}^{(4)}) + 2\dot{f}_2 \dot{\theta} + \frac{1}{Ml} f_2^2 sc - \frac{2}{l} f_2 \dot{l} \dot{\theta} - \frac{g}{l} f_2 s \right), \quad (10)$$

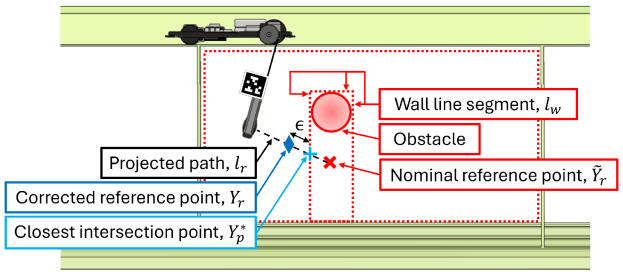

Fig. 5. Illustration of collision prevention algorithm when the nominal reference point (cross), $\tilde{Y}_r$, specified by the operator lies within an obstacle's bounding box. The corrected reference point (diamond), Y_r, is specified at a distance ϵ towards the current position from the closest intersection point (plus), Y_p^*, of the reference line segment (dashed), l_r, and the set of bounding box walls (dotted), L_w.

$$\ddot{f}_{2,ff} = m(s y_{1,d}^{(4)} - c y_{2,d}^{(4)}) + f_2 \dot{\theta}^2 \tag{11}$$

and then integrating twice over time to find the feedforward input $f_{2,ff}$, with initial conditions $f_2(0) = -mg$ and $\dot{f}_2(0) = 0$ when starting from rest. The desired state X_d and feedforward $F_{ff} = [f_{1,ff} \;\; f_{2,ff}]^T$ satisfies the system dynamics

$$\dot{X}_d = f(X_d) + g(X_d) F_{ff} \tag{12}$$

in (1), and the corresponding desired system states X_d can be computed as [13]

$$x_d = y_{1,d} - \frac{\ddot{y}_{1,d} y_{2,d}}{\ddot{y}_{2,d} + g}, \tag{13}$$

$$\dot{x}_d = \dot{y}_{1,d} - \frac{y_{1,d}^{(3)} y_{2,d} + \ddot{y}_{1,d} \dot{y}_{2,d}}{\ddot{y}_{2,d} + g} - \frac{\ddot{y}_{1,d} y_{2,d} y_{2,d}^{(3)}}{(\ddot{y}_{2,d} + g)^2}, \tag{14}$$

$$l_d = \left(\left(\frac{\ddot{y}_{1,d} y_{2,d}}{\ddot{y}_{2,d} + g} \right)^2 + y_{2,d}^2 \right)^{\frac{1}{2}}, \tag{15}$$

$$\dot{l}_d = \left(\left(\frac{\ddot{y}_{1,d} y_{2,d}}{\ddot{y}_{2,d} + g} \right)^2 + y_{2,d}^2 \right)^{-\frac{1}{2}} \left(y_{2,d} \dot{y}_{2,d} + \left(\frac{\ddot{y}_{1,d} y_{2,d}}{\ddot{y}_{2,d} + g} \right) \times \left(\frac{y_{1,d}^{(3)} y_{2,d} + \ddot{y}_{1,d} \dot{y}_{2,d}}{\ddot{y}_{2,d} + g} - \frac{\ddot{y}_{1,d} y_{2,d} y_{2,d}^{(3)}}{(\ddot{y}_{2,d} + g)^2} \right) \right), \tag{16}$$

$$\theta_d = \tan^{-1} \left(\frac{-\ddot{y}_1}{\ddot{y}_2 + g} \right). \tag{17}$$

$$\dot{\theta}_d = \frac{-y_{1,d}^{(3)} (\ddot{y}_{2,d} + g) + \ddot{y}_{1,d} y_{2,d}^{(3)}}{(\ddot{y}_{2,d} + g)^2 + \ddot{y}_{1,d}^2}. \tag{18}$$

(13)–(18) impose the condition of $\ddot{y}_{2,d} > -g$ to maintain positive cable tension and prevent slackening.

B. Stabilizing State Feedback

The crane robot will exactly track any four times differentiable, desired-output trajectory Y_d with the feedforward input F_{ff} in (12). A state feedback $F_{fb} = \begin{bmatrix} f_{1,fb} & f_{2,fb} \end{bmatrix}^T$, needed to stabilize the desired trajectory X_d in response to perturbations, is described next.

Lemma 1 (Stability without time variations): The feedback law

$$F_{fb} = -KX = -\begin{bmatrix} k_1 & k_2 & k_3 & k_4 & 0 & 0 \\ 0 & 0 & 0 & 0 & k_5 & k_6 \end{bmatrix} X, \tag{19}$$

stabilizes the system in (1) about the equilibrium state, $X_{eq} = \begin{bmatrix} x_0 & 0 & 0 & 0 & l_0 & 0 \end{bmatrix}^T$, and corresponding equilibrium input, $F_{eq} = \begin{bmatrix} 0 & -mg \end{bmatrix}^T$, at any given cart position x_0 and positive payload length l_0, by selecting gains as $k_1 > 0, k_2 > 0$, $k_3 < mg$, $k_4 = 0$, $k_5 > 0$, $k_6 > 0$.

Proof: Linearization of the system model in (1) about the equilibrium in the lemma results in

$$\dot{X} = AX + BF, \tag{20}$$

where applying the input as the feedback $F = F_{fb}$ in (19) to (20) with $k_4 = 0$ results in the closed-loop dynamics

$$\dot{X} = \left[\begin{array}{cccc|cc} 0 & 1 & 0 & 0 & 0 & 0 \\ -\frac{k_1}{M} & -\frac{k_2}{M} & \frac{mg-k_3}{M} & 0 & 0 & 0 \\ 0 & 0 & 0 & 1 & 0 & 0 \\ \frac{k_1}{Ml_0} & \frac{k_2}{Ml_0} & \frac{k_3-(M+m)g}{Ml_0} & 0 & 0 & 0 \\ \hline 0 & 0 & 0 & 0 & 0 & 1 \\ 0 & 0 & 0 & 0 & -\frac{k_5}{m} & -\frac{k_6}{m} \end{array}\right] X = \begin{bmatrix} A_1 & 0_{4x2} \\ 0_{2x4} & A_2 \end{bmatrix} X. \tag{21}$$

Conditions on the gains in K for stability can be derived from the blocks, A_1 and A_2, separately. The characteristic equation of A_1 is given by

$$Ml_0\lambda^4 + k_2 l_0 \lambda^3 + (k_1 l_0 - k_3 + (M+m)g)\lambda^2 + k_2 g \lambda + k_1 g = 0 \tag{22}$$

and the conditions for the stability of A_1 can be obtained using the Routh array as $k_1 > 0, k_2 l_0 > 0, k_1 l_0 + (mg - k_3) > 0, \frac{k_2(mg-k_3)}{k_1 l_0 + (mg-k_3)} > 0$ [25]. The characteristic equation for A_2 is given by $m\lambda^2 + k_6 \lambda + k_5 = 0$, resulting in conditions $k_5 > 0$ and $k_6 > 0$ for stability. The lemma follows. ■

Lemma 2 (Stability with time variations): The origin of the error $E = X - X_d$ dynamics with the feedforward input F_{ff} augmented with feedback F_{fb}

$$F = \begin{bmatrix} f_{1,ff} \\ f_{2,ff} \end{bmatrix} + \begin{bmatrix} f_{1,fb} \\ f_{2,fb} \end{bmatrix} = F_{ff} + F_{fb} \tag{23}$$

is stable provided the desired-output trajectories Y_d are sufficiently slowly-varying, i.e., the time derivatives $Y_d^{(i)}$ for $i = \{1, \ldots, 4\}$ are sufficiently small, with sufficiently small deviations in payload length, i.e., $\max_t(|l_d(t) - l_0|)$ is sufficiently small.

Proof: This follows from standard slowly-time-varying arguments. Essentially, the linearization of trajectory tracking has the form $\dot{E}(t) = A(t)E(t) + B(t)F_{fb}(t)$, which can be shown to be a vanishing perturbation of (20), that can be made small under the conditions of the lemma, and $A(t)$ is bounded along with its gradient with respect to the time-varying parameters. See [25] for a detailed proof. ■

Output tracking can be achieved by combining the feedforward (from (12)) and a stabilizing feedback (from (19) with $k_4 = 0$) as

$$f_1 = f_{1,ff} - k_1(x - x_d) - k_2(\dot{x} - \dot{x}_d) - k_3(\theta - \theta_d), \tag{24}$$

IEEE Robotics and Automation Letters (RA-L) paper, presented at ICRA 2026, Vienna, Austria. Cite as RA-L paper.

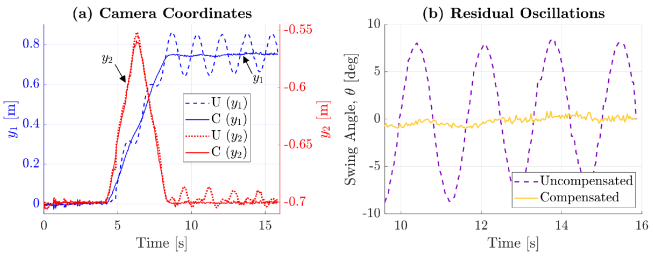

Fig. 6. Tracking comparison (see supplementary material for video) of the fast ramp-like trajectory (transition time of $T_t = 4$ s) described in Section IV with compensated (C) and uncompensated (U) swing dynamics. (a) Horizontal camera position, y_1, and vertical camera position y_2, and (b) residual oscillations at the inspection location.

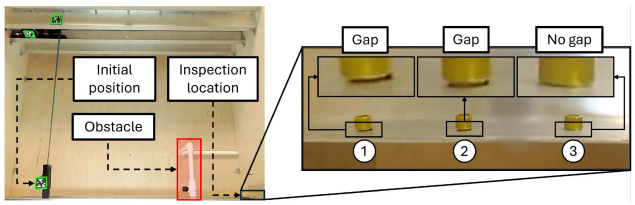

Fig. 7. The experimental setup for the fastener inspection task. Participants move the crane robot from an initial position over the pipeline obstacle to the inspection location with three fasteners. The sample inset image shows fasteners 1 and 2 with gaps (which can be observed visually), while fastener 3 is properly seated and has no gap.

$$f_2 = \left(\iint \ddot{f}_{2,ff}\, d^2t\right) + \dot{f}_2(0)t + f_2(0) - k_5(l - l_d) - k_6(\dot{l} - \dot{l}_d). \tag{25}$$

Remark 1 (Exponential tracking): A specified trajectory-tracking performance, i.e., a desired characteristic equation for the error dynamics, say $\lambda^4 + \sum_{i=0}^{3} a_{k,i}\lambda^i = 0$ where the error is $e_k = y_k - y_{k,d}$, $k \in \{1, 2\}$ can be achieved by selecting the controller v_k, $k \in \{1, 2\}$ as $v_k = y_{k,d}^{(4)} - \sum_{i=0}^{3} a_{1,i}(y_k^{(i)} - y_{k,d}^{(i)})$ [25]. However, this requires higher-order time derivatives of potentially noisy output measurements, which is avoided by the state feedback in (19).

C. Semi-Autonomous Controller

In semi-autonomous control, the operator's reference command (output velocity, $\dot{Y}_r$) from the joystick interface is used to autonomously plan a snap-continuous (i.e., C^4 continuous) trajectory, $Y_d(t)$, designed (i) to avoid collisions, and (ii) to be sufficiently smooth for output tracking using the differential flatness property.

1) Reference Specification: The reference output-velocity, $\dot{Y}_r$, is specified by the operator as $\dot{Y}_r = [\dot{y}_{1,r}\ \dot{y}_{2,r}]^T = [\alpha_1 j_1\ \alpha_2 j_2]^T$, where α_1 and α_2 are gains scaling the joystick inputs, j_1 and j_2, respectively. The velocity reference, $\dot{Y}_r(t)$ at time t is used to define the nominal reference point, $\tilde{Y}_r(t+T)$, to be reached within the time horizon, T, from the current time, t, i.e., $\tilde{Y}_r(t+T) = Y(t) + \dot{Y}_r T$. The nominal reference point $\tilde{Y}_r(t+T)$ acts similar to velocity commands, as larger operator-inputs (j_1, j_2) will generate higher-speed trajectories.

2) Collision Avoidance: Collision is evaluated through projection from the crane robot [26]. Intersection between obstacles and the projected path of the crane robot, l_r, connecting the output, $Y(t)$, to the nominal operator-specified reference point, $\tilde{Y}_r(t+T)$, indicate imminent collision. If the projected path falls inside an obstacle, then a corrected reference point, $Y_r(t+T)$, is selected to be outside the obstacle. Obstacle locations in the manufacturing environment are assumed to be known, so obstacles are modeled by bounding boxes extending to the floor to prevent the camera payload from moving below obstacles, as illustrated in Fig. 5.

An intersection between the projection and an obstacle indicates imminent collision, as the projection predicts that the planned trajectories will pass through the bounding box. The set $L_w = \{l_{w,0}, l_{w,1}, \ldots, l_{w,N}\}$ of N line segments consisting of the confined space's wall line segments and the obstacles' bounding boxes, is checked for collision with the projected reference line segment, l_r. The set of intersection points, $P = \{Y_p \mid Y_p = l_r \cap l_{w,n}, n \in \{0, 1, \ldots, N\}\}$, is used to obtain the corrected reference point, Y_r, located at a distance offset ϵ (to account for disturbance) along the projection, l_r, towards the current state, Y, from the closest intersection point, Y_p^*, if there is an intersection (see Fig. 5), such that

$$Y_r = \begin{cases} Y_p^* - \epsilon \frac{Y_p^* - Y(t)}{|Y_p^* - Y(t)|}, & \text{if } P \neq \varnothing \text{ (intersection)}, \\ \tilde{Y}_r, & \text{if } P = \varnothing \text{ (otherwise)}. \end{cases} \tag{26}$$

where $Y_p^* = \arg\min_{Y_p \in P} \|Y_p - Y(t)\|$.

3) Trajectory Generation: From the corrected reference point, Y_r, a snap-continuous, desired output-trajectory $Y_d(\cdot)$ is planned over the time interval $t \leq \tau \leq t + T$. Five initial boundary conditions at time $\tau = t$ are found from the outputs and time derivatives of the outputs, $Y_d^{(i)}(t)$. Additionally, five final boundary conditions at time $\tau = t + T$ are defined by the corrected reference point as $Y(t+T) = Y_r$, with final output derivatives set to zero (i.e. $\dot{Y}_d(t+T) = \ddot{Y}_d(t+T) = Y_d^{(3)}(t+T) = Y_d^{(4)}(t+T) = 0$) such that all desired trajectories are planned to reach a resting output state in the case of imminent collision [26]. Moreover, selecting the final time trajectory derivatives to zero (especially, $\dot{Y}_d(t+T) = 0, Y_d^{(3)}(t+T) = 0$) results in zero final swing angle $\theta_d(t+T) = 0$ and zero swing-angle velocity $\dot{\theta}_d(t+T) = 0$ from (17) and (18), and thereby, removes residual oscillations at time $t + T$. The minimal order polynomial is ninth-order with ten coefficients, i.e., $c_{k,0}$-$c_{k,9}$, to satisfy the ten boundary conditions on each output trajectory $Y_{k,d}^{(i)}(t)$ and $Y_{k,d}^{(i)}(t+T)$ for $0 \leq i \leq 4$, $k \in \{1, 2\}$. Therefore, the desired trajectory for each output, $y_{k,d}(\tau)$ ($k \in \{1, 2\}$), is selected independently as

$$y_{k,d}(\tau) = c_{k,9}\tau^9 + c_{k,8}\tau^8 + \ldots + c_{k,1}\tau + c_{k,0}. \tag{27}$$

Given the desired output trajectory, Y_d, as in (27) the control inputs, f_1 and f_2, can be found from (24) and (25). Fig. 3 shows a block diagram of the crane robot's control and Algorithm. 1 summarizes the semi-autonomous controller, which generates a new polynomial trajectory at each control timestep based on joystick inputs, similar to [19].

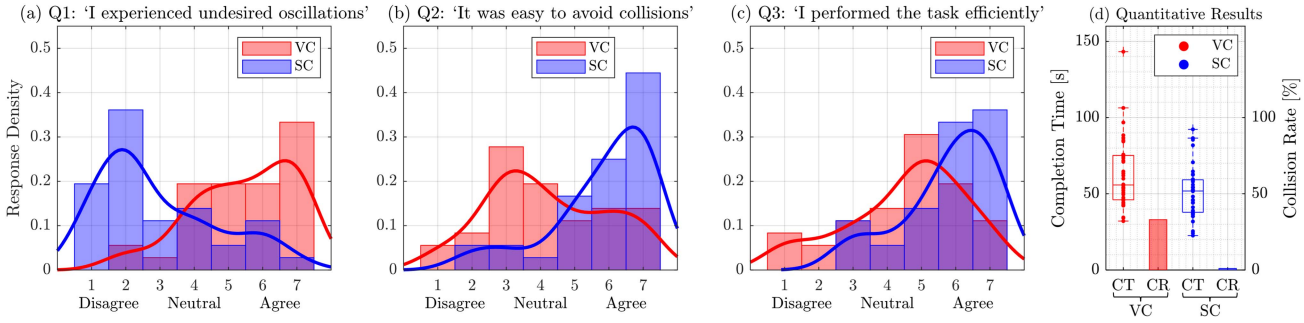

Fig. 8. Results from 36 teleoperated inspection trials. (a)–(c) Histogram of response density from subjective questionnaire on a 7-point Likert scale (1: Strongly disagree; 4: Neutral; 7: Strongly agree) comparing responses collected after using VC (without swing-dynamics compensation) and SC (with swing-dynamics compensation). Solid lines are response-density trends with a squared exponential kernel smoothing (bandwidth of 0.7). (d) Quantitative measures of task completion time (CT) and collision rate (CR) for decoupled velocity control (VC) and semi-autonomous control (SC).

Algorithm 1: Semi-Autonomous Controller.

Given: Input gains α_1, α_2; Time horizon T; Bounding-box line segments L_w; Distance offset ϵ; $i \in \{0, \ldots, 4\}$; Cart mass M; Payload mass m; Feedback gains K
while true do
  Get joystick inputs j_1, j_2
  Get state feedback $X(t)$ from external camera
  $Y_d^{(i)}(t) \leftarrow$ Eqs. (2), (3), (5), (6), (8)
  $\dot{Y}_r \leftarrow \begin{bmatrix}\alpha_1 j_1 & \alpha_2 j_2\end{bmatrix}^T$
  $\tilde{Y}_r \leftarrow Y(t) + \dot{Y}_r T$
  $l_r \leftarrow \overline{Y(t)\tilde{Y}_r}$
  $P \leftarrow \{Y_p \mid Y_p = l_r \cap l_{w,n}, n \in \{0, 1, \ldots, N\}\}$
  $Y_r \leftarrow$ Eq. (26)
  $Y_d^{(i)}(\tau) \leftarrow$ Eq. (27)
  $X_d(\tau) \leftarrow$ Eqs. (13)–(18)
  $f_1, f_2 \leftarrow$Eqs. (24)–(25)
  Apply f_1 and f_2 to actuators
end while

VI. Experimental Results and Discussion

A. Flatness-Based Input Validation

Compensating for the swing dynamics substantially improves tracking of the desired trajectory when compared to the uncompensated case. To illustrate, the proposed flatness-based input in (24) and (25) is applied to the fast ramp-like trajectory presented in Section IV with a transition time of $T_t = 4$ seconds to compensate for the undesired residual oscillations. Fig. 6(a) compares the time trajectories of the uncompensated response (neglecting the swing dynamics) to the compensated response (accounting for swing dynamics) for the horizontal y_1 and vertical y_2 camera positions. The maximum amplitude of the residual oscillations upon reaching the inspection location are reduced by 89%, as the oscillation magnitude remains below 1.0 degrees in the compensated case, compared to 9.1 degrees in the uncompensated case, as shown in Fig. 6(b).

B. User Trials

Evaluated against the conventional industrial gantry crane control approach of decoupled velocity control (VC) [9] without swing-dynamics compensation, which relies on operator compensation of oscillations and collision avoidance, the semi-autonomous control (SC) improved efficiency and safety for 12 participants in a fastener inspection task.

1) Fastener Inspection Task: The fastener inspection task asks participants to move across the confined space over a pipeline obstacle to identify whether three fasteners are properly seated (i.e. no gaps under the fastener), as depicted in Fig. 7. Each participant performed three trials; in each trial, the participant performed the task twice in a single-blind manner, once with VC and once with SC. A pseudorandom number generator specified the order that each controller was used as well as the fastener gap configuration. To complete the task, participants recorded which fasteners contained gaps before capturing an image from the camera payload and confirming task completion. In the event of collision, the task was recorded as a failed attempt, and the participant restarted the task. After each task, participants completed a questionnaire.

2) Experiment Parameters: Experiments were completed by moving the camera payload from rest at initial output coordinates, (y_1, y_2), of $(0, -0.72)$ m to inspect three fasteners seated at $(0.88, -0.72)$ m. The reference velocity, $\dot{Y}_r$ was generated by scaling the joystick inputs, j_1 and j_2 ranging from $[-1, 1]$, by gains $\alpha_1 = 0.12$ and $\alpha_2 = 0.04$, respectively. The cart mass, M, and camera payload mass, m, were 0.815 kg and 0.225 kg, respectively. VC tracked $\begin{bmatrix}\dot{x} & \dot{l}\end{bmatrix}^T = \dot{Y}_r$ using feedback control, while SC applied Algorithm 1 to plan trajectories over a time horizon, $T = 1.5$ s, ensuring trajectories remain in the confined space bounded virtually by $y_1 \in$ [0,0.88] m and $y_2 \in [-0.75, -0.3]$ m and avoided collision with the pipeline obstacle modeled as a bounding box parameterized by $y_1 \in$ [0.575,0.65] m and $y_2 \in [-0.75, -0.5]$ m using a distance offset of $\epsilon = 8$ cm for a conservative buffer. Gains, satisfying conditions in Lemma 1, were experimentally selected by increasing them to improve tracking without oscillations or overshoot as $k_1 = 0.8$ N/mm, $k_2 = 0.8$ N/mm·s, $k_3 = -0.05$ N/rad, $k_4 = 0$ N/rad·s, $k_5 = 0.2$ N/mm, and $k_6 = 0.2$ N/mm·s.

3) Reduced Oscillation: Participants reported a decrease in undesired oscillations when using SC compared to VC, as shown through responses to Q1 in Fig. 8(a), supported by a Wilcoxon signed rank test, which revealed a statistically significant difference between the two controllers, rejecting the null hypothesis ($p < 0.05$). Experiencing an increase in undesired oscillations while using VC compared with SC is consistent with the autonomous experiments of Section VI-A, as VC leaves unaccounted residual oscillations for participants while SC leverages the differential flatness to remove oscillations.

IEEE Robotics and Automation Letters (RA-L) paper, presented at ICRA 2026, Vienna, Austria. Cite as RA-L paper.

4) Safer Inspection: The use of SC resulted in safer inspection for both the crane robot and surrounding aircraft structure with a collision rate of 0% compared to a collision rate of 33% under VC (Fig. 8(d)). The combination of reduced uncontrolled oscillation and reference point corrections led to participants reporting an ease of avoiding collisions through Q2 while using SC compared with VC (Fig. 8(b)). A Wilcoxon signed rank test confirmed this perception, rejecting the null hypothesis ($p < 0.05$).

5) Improved Efficiency: Even neglecting failures due to collisions with VC, SC improved inspection efficiency by reducing mean task completion time by 18.7% (Fig. 8(d)) to 51.2 s compared to a mean task completion time under VC of 63.0 s. A paired-t test demonstrated a statistically significant difference between responses collected from VC and SC, rejecting the null hypothesis ($p < 0.05$). Participants also perceived improved task efficiency using SC as opposed to VC through Q3 of the subjective questionnaire (Fig. 8(c)), where a Wilcoxon signed rank test confirmed this perception, rejecting the null hypothesis ($p < 0.05$).

VII. Conclusion

This work presented a crane robot for teleoperated in-wing confined space inspection. To remove undesired oscillations during teleoperation, the swing dynamics of the crane robot are accounted for by exploiting the differentially-flat dynamics to generate sufficiently smooth trajectories for tracking, while avoiding collision with surrounding obstacles. This enabled semi-autonomous control with reduced undesired oscillations, eliminated collisions, and enhanced inspection efficiency during teleoperation.

Acknowledgment

The authors thank Shuonan Dong and Jonathan Ahn for guidance on the system design.

References

[1] F. Heilemann, A. Dadashi, and K. Wicke, "Eeloscope—Towards a novel endoscopic system enabling digital aircraft fuel tank maintenance," *Aerospace*, vol. 8, no. 5, 2021, Art. no. 136. [Online]. Available: https://www.mdpi.com/2226-4310/8/5/136

[2] N. Guochen, W. Li, G. Qingji, and H. Dandan, "Path-tracking algorithm for aircraft fuel tank inspection robots," *Int. J. Adv. Robot. Syst.*, vol. 11, no. 5, 2014, Art. no. 82.

[3] P. Owan, J. Garbini, and S. Devasia, "Faster confined space manufacturing teleoperation through dynamic autonomy with task dynamics imitation learning," *IEEE Robot. Automat. Lett.*, vol. 5, no. 2, pp. 2357–2364, Apr. 2020.

[4] R. Buckingham et al., "Snake-arm robots: A new approach to aircraft assembly," SAE Technical Paper, Tech. Rep. 2007-01-3870, 2007.

[5] M. K. Dhoot and I.-S. Fan, "Design and development of a mobile robotic system for aircraft wing fuel tank inspection," *SAE Int. J. Adv. Curr. Practices Mobility*, vol. 4, no. 2022-01-0042, pp. 1126–1137, 2022.

[6] Z. Ji, G. Song, F. Wang, Y. Li, and A. Song, "Design and control of a snake robot with a gripper for inspection and maintenance in narrow spaces," *IEEE Robot. Automat. Lett.*, vol. 8, no. 5, pp. 3086–3093, May 2023.

[7] T. Yamamoto, S. Sakama, and A. Kamimura, "Pneumatic duplex-chambered inchworm mechanism for narrow pipes driven by only two air supply lines," *IEEE Robot. Automat. Lett.*, vol. 5, no. 4, pp. 5034–5042, Oct. 2020.

[8] J. Wang et al., "Transformable inspection robot design and implementation for complex pipeline environment," *IEEE Robot. Automat. Lett.*, vol. 9, no. 6, pp. 5815–5822, Jun. 2024.

[9] S. Bonnabel and X. Claeys, "The industrial control of tower cranes: An operator-in-the-loop approach [applications in control]," *IEEE Control Syst. Mag.*, vol. 40, no. 5, pp. 27–39, Oct. 2020.

[10] M. Rubagotti, T. Taunyazov, B. Omarali, and A. Shintemirov, "Semi-autonomous robot teleoperation with obstacle avoidance via model predictive control," *IEEE Robot. Automat. Lett.*, vol. 4, no. 3, pp. 2746–2753, Jul. 2019.

[11] T. Singh and W. Singhose, "Input shaping/time delay control of maneuvering flexible structures," in *Proc. 2002 Amer. Control Conf.*, 2002, pp. 1717–1731.

[12] M. Fliess, J. Lévine, P. Martin, and P. Rouchon, "Flatness and defect of non-linear systems: Introductory theory and examples," *Int. J. Control*, vol. 61, no. 6, pp. 1327–1361, 1995.

[13] B. Kolar and K. Schlacher, "Flatness based control of a gantry crane," *IFAC Proc. Volumes*, vol. 46, no. 23, pp. 487–492, 2013.

[14] B. Kolar, H. Rams, and K. Schlacher, "Time-optimal flatness based control of a gantry crane," *Control Eng. Pract.*, vol. 60, pp. 18–27, 2017.

[15] Z. Yu and W. Niu, "Flatness-based backstepping antisway control of underactuated crane systems under wind disturbance," *Electronics*, vol. 12, no. 1, 2023, Art. no. 244.

[16] J. Zeng, P. Kotaru, M. W. Mueller, and K. Sreenath, "Differential flatness based path planning with direct collocation on hybrid modes for a quadrotor with a cable-suspended payload," *IEEE Robot. Automat. Lett.*, vol. 5, no. 2, pp. 3074–3081, Apr. 2020.

[17] C. Hebisch, S. Jackisch, D. Moormann, and D. Abel, "Flatness-based model predictive trajectory planning for cooperative landing on ground vehicles," in *Proc. 2021 IEEE Intell. Veh. Symp. (IV)*, 2021, pp. 1031–1036.

[18] E. Tal, G. Ryou, and S. Karaman, "Aerobatic trajectory generation for a VTOL fixed-wing aircraft using differential flatness," *IEEE Trans. Robot.*, vol. 39, no. 6, pp. 4805–4819, Dec. 2023.

[19] M. Thomas, T. Werner, and O. Sawodny, "Online trajectory generation and feedforward control for manually-driven cranes with input constraints," in *Proc. 2021 IEEE Conf. Control Technol. Appl.*, 2021, pp. 654–659.

[20] Y. Gao, G. Song, S. Li, F. Zhen, D. Chen, and A. Song, "LineSpyX: A power line inspection robot based on digital radiography," *IEEE Robot. Automat. Lett.*, vol. 5, no. 3, pp. 4759–4765, Jul. 2020.

[21] D. Rakita, B. Mutlu, and M. Gleicher, "An autonomous dynamic camera method for effective remote teleoperation," in *Proc. 2018 ACM/IEEE Int. Conf. Hum.-Robot Interact.*, 2018, pp. 325–333.

[22] E. Olson, "AprilTag: A robust and flexible visual fiducial system," in *Proc. IEEE Int. Conf. Robot. Automat.*, 2011, pp. 3400–3407.

[23] Y. Nishimura, S. Takahashi, H. Mochiyama, and T. Yamaguchi, "Automated hammering inspection system with multi-copter type mobile robot for concrete structures," *IEEE Robot. Automat. Lett.*, vol. 7, no. 4, pp. 9993–10000, Oct. 2022.

[24] Z. Yu, J. Luo, H. Zhang, E. Onchi, and S.-H. Lee, "Approaches for motion control interface and tele-operated overhead crane handling tasks," *Processes*, vol. 9, no. 12, 2021, Art. no. 2148.

[25] W. Marquette, K. Schultz, V. Jonnalagadda, B. Wong, J. Garbini, and S. Devasia, "Semi-autonomous teleoperation using differential flatness of a crane robot for aircraft in-wing inspection: Extended version," 2024, *arXiv:2412.10973*.

[26] X. Yang, J. Cheng, and N. Michael, "An intention guided hierarchical framework for trajectory-based teleoperation of mobile robots," in *Proc. 2021 IEEE Int. Conf. Robot. Automat.*, 2021, pp. 482–488.